JACS
JOURNAL OF THE AMERICAN CHEMICAL SOCIETY
pubs.acs.org/JACS
Article

Breaking a Molecular Scaling Relationship Using an Iron−Iron Fused Porphyrin Electrocatalyst for Oxygen Reduction

Daiki Nishiori, Jan Paul Menzel, Nicholas Armada, Edgar A. Reyes Cruz, Brent L. Nannenga, Victor S. Batista, and Gary F. Moore*

Cite This: J. Am. Chem. Soc. 2024, 146, 11622−11633
Read Online
ACCESS | Metrics & More | Article Recommendations | Supporting Information

ABSTRACT: The design of efficient electrocatalysts is limited by scaling relationships governing trade-offs between thermodynamic and kinetic performance metrics. This *"iron law"* of electrocatalysis arises from synthetic design strategies, where structural alterations to a catalyst must balance nucleophilic versus electrophilic character. Efforts to circumvent this fundamental impasse have focused on bioinspired applications of extended coordination spheres and charged sites proximal to a catalytic center. Herein, we report evidence for breaking a molecular scaling relationship involving electrocatalysis of the oxygen reduction reaction (ORR) by leveraging ligand design. We achieve this using a binuclear catalyst (a diiron porphyrin), featuring a macrocyclic ligand with extended electronic conjugation. This ligand motif delocalizes electrons across the molecular scaffold, improving the catalyst's nucleophilic and electrophilic character. As a result, our binuclear catalyst exhibits low overpotential and high catalytic turnover frequency, breaking the traditional trade-off between these two metrics.

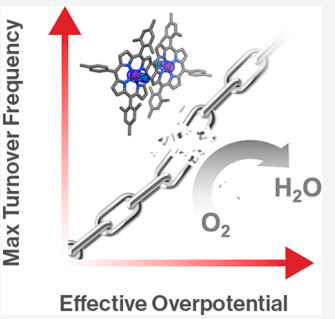

INTRODUCTION

Catalysts are essential to the efficient performance of technological systems and all living organisms. However, molecular scaling relationships[1−4] involving trade-offs between thermodynamic and kinetic performance metrics can limit their effectiveness. The Sabatier principle[5,6] indicates that optimal catalysis occurs when the binding between a catalyst and its substrate is *"just right"* and of intermediary strength. In other words, the interactions should be neither too strong nor too weak; otherwise, the binding of the reactants or desorption of the products will limit the reaction rate. Such trade-offs between thermodynamic and kinetic performance metrics also apply to electrocatalytic reactions, as exemplified in the benchmarking of homogeneous molecular electrocatalysts via comparisons of catalytic Tafel plots[7,8] relating the turnover frequency (TOF) of a molecular catalyst to the overpotential (η) (Figure 1a). In this analysis, TOF is the ratio of moles of product ($N_{product}$) produced over a set unit of time, in which the catalyst is stable, versus the moles of total catalysts contained within the *reaction-diffusion layer* (N_{cat}), a region near the electrode surface, where the concentration profiles of electro-activated versus nonactivated catalysts differ from their bulk values (eq 1).[8] Correspondingly, η is defined as the difference in absolute value between the applied electrode potential (E_{app}) and the equilibrium potential of the reaction being catalyzed (E_{eq}; eq 2).[9−11]

$$\mathrm{TOF} = \frac{N_{\mathrm{product}}}{N_{\mathrm{cat}}} = \frac{\mathrm{TOF}_{\max}}{1 + \exp\left[\frac{F}{RT}(E_{\mathrm{app}} - E_{\mathrm{cat}/2})\right]} \quad (1)$$

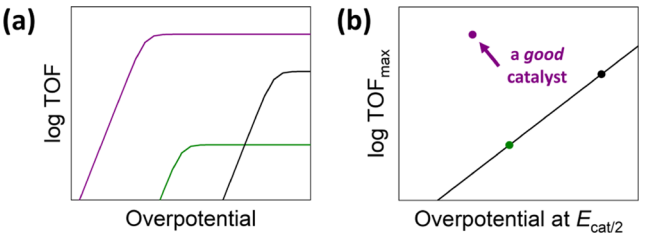

Figure 1. (a) Examples of catalytic Tafel plots and (b) a plot correlating the associated maximum turnover frequencies (TOF_{max}) and overpotentials required to achieve half the maximum turnover frequency ($E_{cat/2}$). A *good* catalyst appears off the correlation line showing a traditional scaling relationship.

$$\eta = |E_{\mathrm{eq}} - E_{\mathrm{app}}| \quad (2)$$

When the activity of an electrocatalyst is limited only by kinetics associated with the consumption of chemical substrates—and not by the rate of electron transfer between the electrode and catalysts or mass-transfer phenomena—the catalysts at the electrode surface are effectively all in their activated form. In addition, the concentration of chemical substrates at the electrode surface will be approximately equal

Received: August 8, 2023
Revised: February 17, 2024
Accepted: February 22, 2024
Published: April 19, 2024

https://doi.org/10.1021/jacs.3c08586
J. Am. Chem. Soc. 2024, 146, 11622−11633

to their bulk values.[7,8,12−14] Under these conditions, the plateau currents recorded during a voltammogram trace will not increase if the applied bias potential or scan rate is increased because the activated catalysts operate at their maximum turnover frequency (TOF_{max}).

For most catalytic reaction mechanisms where the reaction is first order in catalyst, TOF_{max} is equal to the observed rate constant (k_{cat}), which is a global rate constant (with units of s^{-1}) representing either a composite of constants for the elementary steps of the catalytic cycle or the rate constant for a rate-limiting step. As expressed in eq 3, k_{cat} is the product of the concentration of the chemical substrate (C_A^0) and a rate constant for catalysis (k'_{cat}, with units of $mol^{-x}\ L^x\ s^{-1}$), which takes into account the order of the reaction (x) with respect to C_A^0.[8] The relationship between TOF_{max} and TOF is indicated in eq 1, where F is the Faraday constant, R is the gas constant, and T is the temperature. Unlike TOF (a potential-dependent value), TOF_{max} is a potential-independent constant providing a kinetic benchmarking parameter.

$$TOF_{max} = k_{cat} = k'_{cat}[C_A^0]^x \quad (3)$$

The value of TOF_{max} also establishes a related thermodynamic benchmarking parameter termed $E_{cat/2}$, which is the half-wave potential of a steady-state catalytic wave and thus the potential required to achieve half the maximum TOF.[15] By extension, $E_{cat/2}$ is the electrode potential, where half of the catalysts at the electrode surface are present in their activated form. As shown in eq 4, the difference in absolute value between $E_{cat/2}$ and E_{eq} yields the effective overpotential (η_{eff}),[15] which corresponds to the "elbow" of a catalytic Tafel plot.[11]

$$\eta_{eff} = |E_{eq} - E_{cat/2}| \quad (4)$$

The benchmarking of catalysts using catalytic Tafel plots has revealed a general trend referred to as an *"iron law"* of electrocatalysis where, for a selected electrochemical transformation and chemical substrate concentration, there is a linear relationship governing trade-offs between the TOF_{max} and $E_{cat/2}$ parameters (see Figure 1).[16−20] This molecular scaling relationship is rationalized in terms of structure−activity relationships, where changes that alter the electrophilicity of an electrocatalyst to enhance the electron-transfer energetics adversely affect the basicity/nucleophilicity of the electrocatalyst. This results in less favorable kinetics for chemical steps involving the binding of protons or other electrophiles that are essential reagents in most fuel-forming reactions and solar photochemistry.[21−23] Although using electron-withdrawing or electron-donating substituents can provide Marcusian control[24,25] over both the kinetics and thermodynamics of charge-transfer reactions involving electron donor−acceptor interactions, this strategy is fundamentally limited for electrocatalytic reactions, necessitating the pairing of electron transfer with bond breaking/forming chemical steps (including sequential or concerted proton-coupled electron transfer pathways).[26−28] To circumvent this problem, new strategies for designing effective electrocatalysts are needed.[29,30] Promising approaches include using extended coordination spheres[31−35] for managing and stabilizing transition states throughout multisubstrate catalytic cycles, using Coulombic interaction, including substituent groups bearing cationic charges, for stabilizing reaction intermediates,[36−38] and using two different ligands to control reduction potentials and the kinetics of chemical steps.[39,40] More recently, it has been postulated that catalysts featuring ligands with extended π-conjugation[41] (including binuclear complexes) may provide an alternate but complementary approach to breaking scaling relationships in molecular electrocatalysis; however, results supporting this have been limited.[42−46] In the case of binuclear fused porphyrin complexes,[42,45,47,48] promising features include (1) more than one metallic site, (2) a π-extended ligand environment capable of delocalizing electrons across the multimetallic scaffold, and (3) the ability to store multiple reducing equivalents.

In this article, we report comparisons of molecular Tafel plots constructed for chloro[5,10,15,20-tetrakis(4-methylphenyl)porphyrinato]iron(III) ([FeTTP]Cl), a known monometallic-site porphyrin catalyst for the oxygen reduction reaction (ORR), versus a binuclear fused iron(III) porphyrin, featuring an extended π-conjugated macrocycle ($[Fe_2FP]Cl_2$) (Chart 1 and Figure 2), and present evidence for breaking a molecular scaling relationship. In addition, we also report—for the first time—on the crystallographic structure of $[Fe_2FP]Cl_2$ obtained via microcrystal electron diffraction (MicroED)[49] and on the geometries and spin states of the complex in the solution phase as determined via computational analysis.

Chart 1. Molecular Structures of $[Fe_2FP]Cl_2$ (Left) and [FeTTP]Cl (Right)

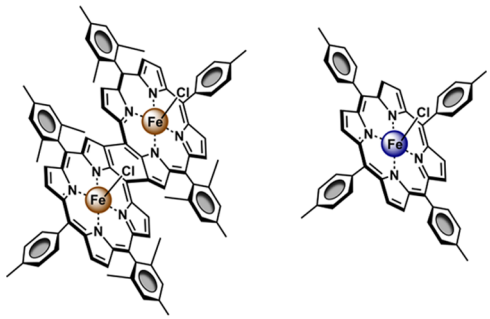

RESULTS AND DISCUSSION

MicroED Crystal Structure. To study the structure of $[Fe_2FP]Cl_2$, we used the cryogenic electron microscopy method of MicroED, which can determine high-resolution structures directly from small quantities of micro and nanocrystalline materials.[50] The structure determined using a solid, crystalline sample of $[Fe_2FP]Cl_2$ confirms the overall organization of the molecule, showing the chlorine atoms bound to each iron atom at a distance of 2.25 Å and on alternate sides of the planar porphyrin macrocyclic ligand (Figures 2b and 2c). Additionally, the iron atom is positioned 0.52 Å above the plane of the porphyrin nitrogens and 0.60 Å above the plane of the macrocyclic ligand. The average Fe−N distance is 2.13 ± 0.01 Å (N = 4). These results indicate that the individual porphyrin units of the fused complex share some structural similarities with previously reported monometallic iron(III) porphyrins;[51] however, the distance between the iron centers in the fused porphyrin is 9.08 Å.

Computational Analysis of Structure and Energetics. Although the MicroED structure gives direct evidence of the conformation in the highly ordered crystalline phase, the catalyst's structure in solution could deviate. We therefore

https://doi.org/10.1021/jacs.3c08586
J. Am. Chem. Soc. 2024, 146, 11622−11633

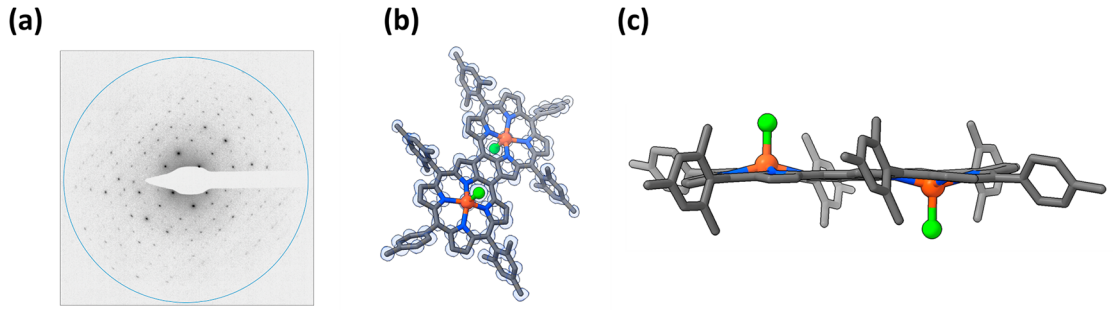

Figure 2. (a) Example diffraction image from the MicroED data sets collected using $[Fe_2FP]Cl_2$ is shown, where the ring represents a resolution of 0.90 Å. (b) The quality of the resulting MicroED structure can be seen in the potential map calculated for the final refined structure. The potential map (blue) is contoured at 2σ. (c) Side view of the $[Fe_2FP]Cl_2$ structure showing the iron atoms slightly out of the plane formed by the porphyrin rings. All diffraction data were collected using $[Fe_2FP]Cl_2$ microcrystals, and data from four well-diffracting crystals were merged for final structure determination.

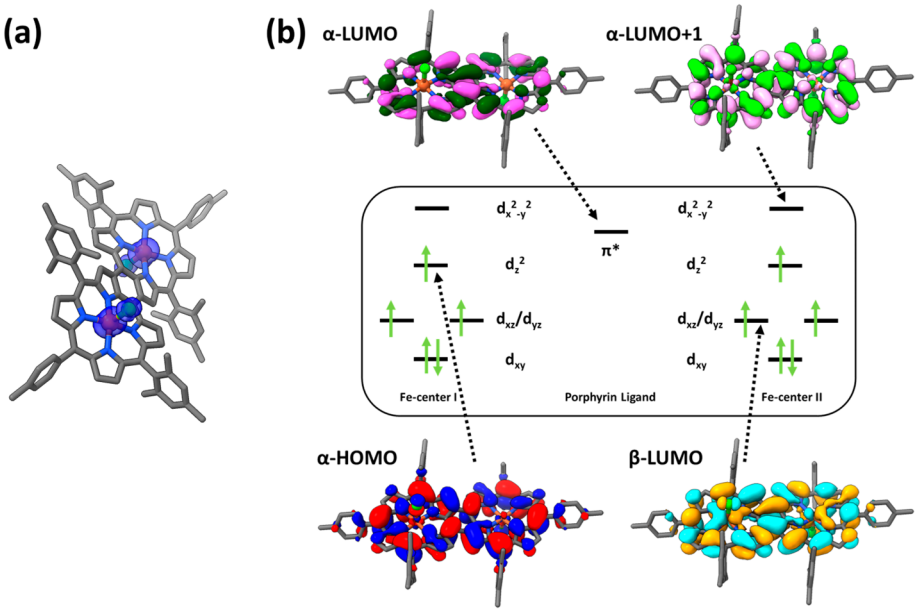

Figure 3. (a) DFT geometry overlaid with the spin density as shown in blue on the $[Fe_2FP]Cl_2$ complex. (b) Molecular orbitals of the $[Fe_2FP]Cl_2$ complex, showing contributions of specific d-orbitals. The inset includes a schematic of the simplified ligand field splitting in a pyramidal environment with the metal positioned out of the plane. The α-LUMO is a ligand-based orbital due to the lowering of the π^* orbital's energetics via extended conjugation.

performed a computational analysis of the $[Fe_2FP]Cl_2$ complex in an implicit solvent. This approach also provides information on the spin-state energetics. Our calculations indicate that the septet spin state is the most stable state when an implicit solvent (*N*,*N*′-dimethylformamide, DMF) is used (see Table S4). Figure 3a shows a density functional theory (DFT)-optimized structure of $[Fe_2FP]Cl_2$ in the septet spin state and a configuration where both axial chloride ligands are on opposite faces of the porphyrin macrocyclic ligand. Although a stable conformation more closely resembling the crystal structure was arrived at computationally (see Figures S13a and S13b), we also found a slightly lower energy conformation in an implicit solvent (Δ = 97 meV/9.4 kJ mol^{-1}, see Table S5). In comparison with the higher energy conformation, the lower energy conformation displays an out-of-plane deformation of the fused porphyrin macrocycle, where the mesityl groups point toward the axial chloride ligands of the iron porphyrin ring they are attached to, the methylphenyl groups point in opposite directions with respect to each other, and the Fe centers maintain an out-of-plane displacement (see Figure S13c). The differences between the solid- versus solution-phase structures indicated via computational analysis may arise from distinctions associated with the environments of these phases, including differences in molecular dipole moments (see Section 4 of the Supporting Information (SI) on "Computational analysis"). However, the relatively small differences in energy and intrinsic approximations in DFT complicate a definitive determination.

As further depicted in Figure 3a, our computational analysis indicates that the six unpaired electrons of the $[Fe_2FP]Cl_2$ septet state are localized on the two ferromagnetically coupled Fe centers, with each center harboring three unpaired electrons (Mulliken spins of Fe: 2.75 and Cl: 0.24). In accord with the ligand field splitting of a pyramidal environment with the metal center plucked out of the ligand plane, the unpaired electrons localized on the Fe centers and chloride ligands involve a

https://doi.org/10.1021/jacs.3c08586
J. Am. Chem. Soc. 2024, 146, 11622−11633

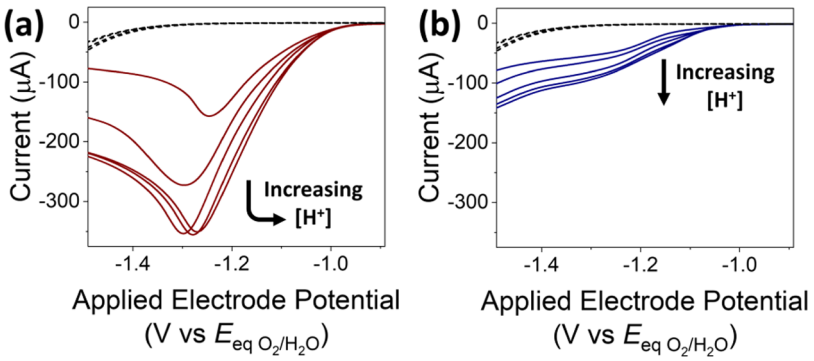

Figure 4. (a) and (b) Voltammograms recorded under O_2 (1 atm) using *N*,*N*′-dimethylformamide solutions containing increasing amounts of $[DMFH^+][OTf^-]$ as a proton source (10, 20, 50, 70, and 100 mM) and either $[Fe_2FP]Cl_2$ (0.30 mM) (panel a, red) or [FeTTP]Cl (0.30 mM) (panel b, blue) as a catalyst. Voltammograms recorded in the absence of a catalyst (black dash) are included for comparison. All data were recorded at a scan rate of 100 mV s^{-1} and using solutions containing $TBAPF_6$ (0.1 M) as a supporting electrolyte.

seemingly linear combination of the d_{z^2}, d_{xz}, and d_{yz} orbitals of the iron and the p_z orbital of the chloride. This results in the d_{xy} orbital being the lowest in energy and doubly occupied, degenerate d_{xz} and d_{yz} orbitals being singly occupied, the d_{z^2} orbital being higher in energy than the d_{xz} and d_{yz} orbitals and singly occupied, and the $d_{x^2-y^2}$ being the most destabilized and unoccupied. This configuration is further supported by the d_{z^2} contribution to the α-HOMO (which is the highest singly occupied orbital, shown in Figure 3b together with a simplified scheme of the d-orbital splitting), the β-LUMO (which shows contributions from d_{xz} or d_{yz}), and the α-LUMO+1 (which shows contributions from $d_{x^2-y^2}$).

Monometallic iron porphyrin complexes structurally similar to [FeTTP]Cl are reported to exist in a high spin state configuration.[52] However, deformation and hydrogen bonding make conversion to intermediate, quartet states possible.[53,54] We find, in our calculations, that the sextet (high spin) and quartet (intermediate spin) states of [FeTTP]Cl are nearly isoenergetic (see Figure S14 and Table S6). This showcases how sensitive the spin-state energetics of these complexes are to their connectivity and microenvironments. Nonetheless, for the fused bimetallic porphyrin $[Fe_2FP]Cl_2$, our calculations show that the intermediate septet spin state is significantly stabilized in comparison to all other spin states (see Table S4). This discrepancy between the spin-state energetics of [FeTTP]Cl versus $[Fe_2FP]Cl_2$ can be explained by the significant stabilization of the π^* orbital (*i.e.*, the α-LUMO) via extended conjugation, which favors intermediate spin states.[53] The lowering of the π^* orbital energy enables stronger back bonding and concomitant stabilization of all d-orbitals with *z* components (including the d_{xz}, d_{yz}, and d_{z^2} orbitals). The lowering of the π^* orbital energy via extended conjugation furthermore results in this energy level dropping below the $d_{x^2-y^2}$ orbital energy, which is a significant difference compared to the energetics of [FeTTP]Cl. This distinction in the electronic structures of [FeTTP]Cl versus $[Fe_2FP]Cl_2$ would manifest as a difference in the redox properties of these complexes. In the case of [FeTTP]Cl, a metal-centered reduction is favored. Conversely, in the case of $[Fe_2FP]Cl_2$, a ligand-centered reduction could be more prominent. This divergence in "*redox-innocent*" versus "*-guilty*" ligand chemistry may play an important role regarding the different electrocatalytic ORR properties of the fused bimetallic versus monometallic porphyrin complexes reported herein and will be investigated by leveraging *in silico* mechanistic studies in future work.

Although the crystal structure of $[Fe_2FP]Cl_2$ determined using the MicroED method shows the two chlorides on opposing faces of the molecular plane, this may not be the energetically preferred geometry when the complex is solvated. Thus, we also determined the structure and energy of the $[Fe_2FP]Cl_2$ configuration with both chlorides on the same face of the porphyrin plane (*syn* configuration) to compare to the $[Fe_2FP]Cl_2$ configuration with the chlorides on opposite faces of the porphyrin plane (*anti* configuration). Our computational results show that in an implicit solvent of DMF, the energy difference between the $[Fe_2FP]Cl_2$ *syn* configuration and *anti* configuration is 73 meV/7.0 kJ mol^{-1} (see Table S4). The calculations therefore agree with the crystal structure, at least in the case of DMF solutions, where an *anti* configuration is energetically more accessible.

Electrocatalytic Performance under Varying Chemical Substrate Concentrations. The electrocatalytic performance of $[Fe_2FP]Cl_2$ and, for enabling comparisons, [FeTTP]Cl was investigated under 1 atm of O_2 using DMF as a solvent, the triflate salt of protonated DMF ($[DMFH^+][OTf^-]$) as a proton source, and 0.1 M tetrabutylammonium hexafluorophosphate ($TBAPF_6$) as a supporting electrolyte. All voltammograms were recorded by using an electrochemical cell equipped with a glassy carbon working electrode wired in a three-electrode configuration. The equilibrium potentials for ORR ($E_{eq\ O_2/H_2O}$ and $E_{eq\ O_2/H_2O_2}$) in DMF with a proton source (HA) are indicated in eqs 5 and 6.[11]

$$O_{2(DMF)} + 4HA_{(DMF)} + 4e^- \rightleftarrows 2H_2O_{(DMF)} + 4A^-_{(DMF)}$$

$$E_{eq\ O_2/H_2O(DMF)}(\text{V vs } Fc^+/Fc) = +0.60 - \frac{0.0592}{4}\log\frac{[H_2O]^2[A^-]^4}{P_{O_2}[HA]^4} - 0.0592pK_{a(HA)} \quad (5)$$

$$O_{2(DMF)} + 2HA_{(DMF)} + 2e^- \rightleftarrows H_2O_{2(DMF)} + 2A^-_{(DMF)}$$

$$E_{eq\ O_2/H_2O_2(DMF)}(\text{V vs } Fc^+/Fc) = +0.06 - \frac{0.0592}{2}\log\frac{[H_2O_2][A^-]^2}{P_{O_2}[HA]^2} - 0.0592pK_{a(HA)} \quad (6)$$

https://doi.org/10.1021/jacs.3c08586
J. Am. Chem. Soc. 2024, 146, 11622−11633

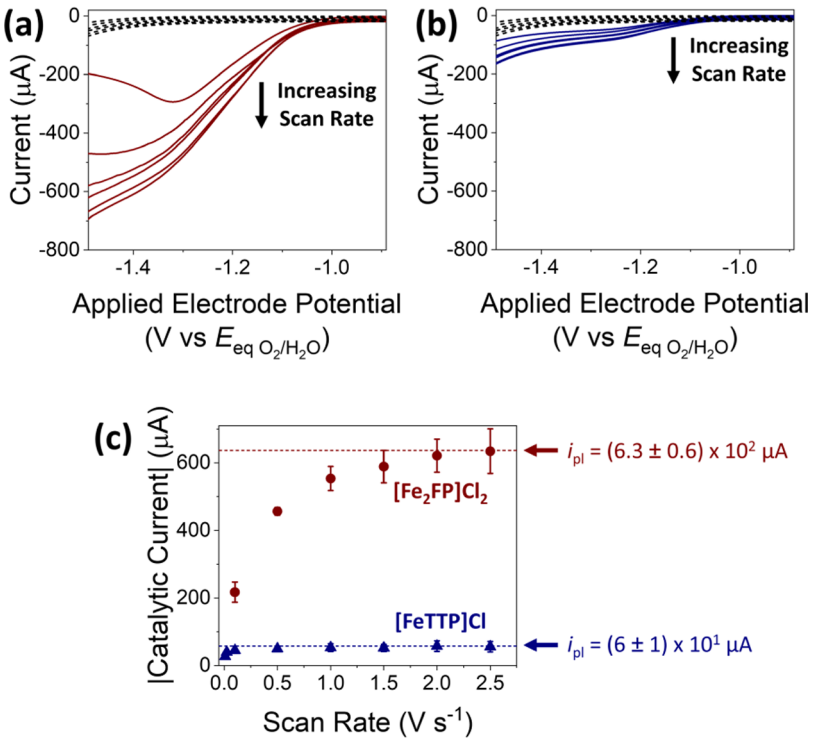

Figure 5. (a) and (b) Voltammograms recorded under O_2 (1 atm) and at increasing scan rates (100, 500, 1000, 1500, 2000, and 2500 mV s^{-1}) using *N,N'*-dimethylformamide solutions containing either $[Fe_2FP]Cl_2$ (0.14 mM) (panel a, red) or [FeTTP]Cl (0.14 mM) (panel b, blue) as a catalyst. Voltammograms recorded in the absence of a catalyst (black dash) are included for comparison. All solutions contained $[DMFH^+][OTf^-]$ (100 mM) as a proton source and $TBAPF_6$ (0.1 M) as a supporting electrolyte. (c) Catalytic current versus scan rate plots obtained from voltammetry measurements using either $[Fe_2FP]Cl_2$ (0.14 mM) (red circles) or [FeTTP]Cl (0.14 mM) (blue triangles) as a catalyst. The catalytic currents are reported at potentials determined via analysis of the first derivative of corresponding voltammograms (see the Experimental Section for details). At sufficiently high scan rates, these currents approach scan-rate-independent values indicated by the dashed horizontal lines labeled catalytic plateau current (i_{pl}). The error bars indicate standard deviations obtained from triplicate measurements (see the SI).

Voltammograms recorded using 0.30 mM solutions of $[Fe_2FP]Cl_2$ in the presence of increasing concentrations of $[DMFH^+][OTf^-]$ (ranging from 10 to 100 mM) display a *peak-shaped* cathodic wave that reaches an acid-concentration-independent, limiting current intensity before shifting to less negative peak potentials at the higher acid concentrations (~50 to 100 mM in $[DMFH^+][OTf^-]$; Figure 4a). These results are consistent with conditions where the current becomes limited by diffusion of O_2.[12,55] At the higher acid concentrations, the anodic shifting of the peak feature is attributed to the more rapid consumption of substrate O_2. In other words, the catalytic TOF increases with acid concentration and the concentration of O_2 near the electrode surface becomes depleted earlier in the voltammogram scan. These results are in stark contrast to those obtained using [FeTTP]Cl as the catalyst (Figure 4b). Rather than a peak-shaped feature that increases in intensity and then shifts to less-biased electrode potentials with increasing acid concentration, the voltammograms recorded using [FeTTP]Cl display a *plateau-shaped* cathodic wave at lower and higher acid concentrations. These results indicate conditions where the consumption of chemical substrates by the catalysts limits the electrocatalytic activity.[12,55] However, currents arising from uncatalyzed O_2 reduction at the glassy carbon electrode surface—as observed in control experiments performed in the absence of an added catalyst (black dashed lines in Figures 4a, 4b, and S15)—are prominent upon polarizing the working electrode more negative than ~ −1.6 V versus the O_2/H_2O equilibrium potential ($E_{eq\ O_2/H_2O}$; Figure S15).

Following the linear sweep voltammetry experiments used to obtain data shown in Figure 4a, the glassy carbon working electrode was rinsed with DMF containing 0.1 M $TBAPF_6$ to remove any physisorbed species before immersing the electrode in a fresh solution of DMF sparged with oxygen (1 atm) and containing 20 mM $[DMFH^+][OTf^-]$ as a proton source and 0.1 M $TBAPF_6$ as a supporting electrolyte. Voltammograms recorded using these rinsed electrodes show no additional current observed beyond the background recorded using a freshly polished glassy carbon working electrode under the otherwise identical experimental conditions, indicating the absence of heterogeneous, electrodeposited catalysts[56−58] (see Figure S16).

Electrocatalytic Performance under Varying Scan Rates. To construct catalytic Tafel plots and better understand our results recorded in the presence of varying concentrations of acid (Figure 4), we investigated the scan rate dependence of voltammogram waveforms recorded using either $[Fe_2FP]Cl_2$ or [FeTTP]Cl (Figure 5). In these experiments, the relative thickness of the *diffusion layer*—the region in the vicinity of an electrode where the concentration of chemical substrates differs from their bulk values[41]—depends on the time scale of the voltammogram scan (*i.e.*, the experimental scan rate). At faster scan rates, the thickness of the diffusion layer is relatively narrower, enabling fluxes of chemical substrates and currents higher than those recorded at slower scan rates and when diffusion of chemical substrates limits the electrocatalytic activity.

https://doi.org/10.1021/jacs.3c08586
J. Am. Chem. Soc. 2024, 146, 11622−11633

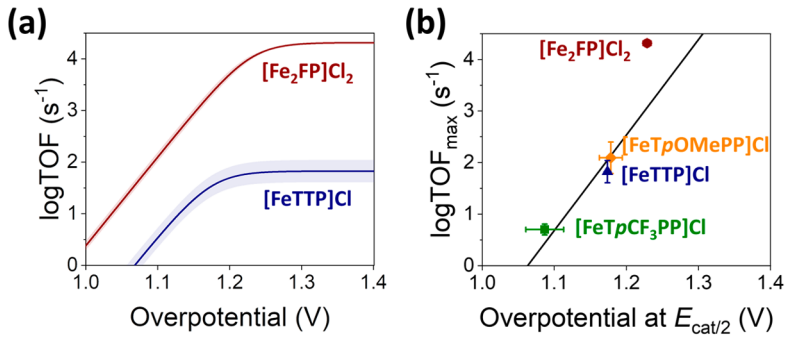

Figure 6. (a) Catalytic Tafel plots constructed from the values of TOF_{max} and $E_{cat/2}$ recorded using *N,N′*-dimethylformamide solutions containing either $[Fe_2FP]Cl_2$ (red) or [FeTTP]Cl (blue) in the presence of O_2 (1 atm), $[DMFH^+][OTf^-]$ (100 mM), and $TBAPF_6$ (0.1 M). The shaded areas indicate standard deviations from the mean values. Overpotential is calculated using a 20 mM concentration of water in *N,N′*-dimethylformamide. (b) $logTOF_{max}$ versus overpotential at $E_{cat/2}$ plot constructed using data included in panel a for $[Fe_2FP]Cl_2$ (red circle) and [FeTTP]Cl (blue triangle). Data obtained using chloro[5,10,15,20-tetrakis[4-(trifluoromethyl)phenyl]porphyrinato]iron(III) ([FeT*p*CF_3PP]Cl), a porphyrin catalyst featuring electron-withdrawing fluorine groups, (green square) or chloro[5,10,15,20-tetrakis(4-methoxyphenyl)porphyrinato]-iron(III) ([FeT*p*OMePP]Cl), a porphyrin catalyst featuring electron-donating methoxy groups, (orange diamond) are included for comparison. The error bars indicate the standard deviations from the mean values. The black line with a slope of 54 mV/dec indicates a traditional scaling relationship for benchmarking a related series of iron porphyrin oxygen reduction reaction catalysts.[16,63−66]

Figures 5a and 5b show voltammograms recorded under 1 atm of O_2 and with increasing scan rates (from 100 to 2500 mV s^{-1}). For these measurements, relatively high concentrations of chemical substrates with respect to the catalysts (*i.e.*, 100 mM $[DMFH^+][OTf^-]$ and 3.1 mM O_2[11,59] versus 0.14 mM in either $[Fe_2FP]Cl_2$ or [FeTTP]Cl as the catalyst) were used to further disfavor the depletion of the chemical substrate concentrations at the electrode surface during experiments performed at the relatively higher range of scan rates.[7,8,12−14] Under these conditions, the voltammograms recorded using $[Fe_2FP]Cl_2$ display a peak-shaped cathodic wave, with an initially scan-rate-dependent intensity, which transforms to a plateau-shaped wave at the higher scan rates and approaches a scan-rate-independent limiting value (Figures 5a and 5c). By contrast, the voltammograms recorded using [FeTTP]Cl in place of $[Fe_2FP]Cl_2$ display an initially plateau-shaped cathodic wave rather than a peak-shaped feature (Figure 5b). Nonetheless, the catalytic currents recorded within the plateau-shaped region also approach scan-rate-independent limiting values upon increasing the scan rate, albeit at relatively lower limiting current intensities and scan rate requirements (Figure 5c). Background currents arising from uncatalyzed O_2 reduction at glassy carbon electrodes (black dashed lines in Figures 5a, 5b, S17, and S18) have been reported to complicate the observation of ideal S-shaped waveforms and the determination of TOF_{max} values without accounting for these background currents via collecting voltammograms recorded in the absence of an added catalyst.[60,61] For this reason and as indicated in Figure 5c, currents recorded using no added catalysts were subtracted from those recorded using an added catalyst to yield the *catalytic current*.

The catalytic plateau currents (i_{pl} values) measured when the electrocatalytic activity is not limited by the rate of electron transfer between the electrode and catalysts or mass-transfer phenomena enable the determination of related TOF_{max} values via analysis of i_{pl}/i_p ratios (eqs 7 and 8),[7,8,12−14] where i_p is a peak current measured in the absence of a chemical substrate (see the Experimental Section for further details).

$$\frac{i_{pl}}{i_p} = \frac{n_{cat}}{0.4463 n_p^{3/2}} \sqrt{\frac{RTk_{cat}}{Fv}} \tag{7}$$

$$k_{cat} = TOF_{max} = 0.4911 v \left(\frac{i_{pl}}{i_p}\right)^2 \tag{8}$$

Benchmarking of Catalysts Using Catalytic Tafel Plots. Surmising a mechanism where initial electron transfer is followed by a rate-determining chemical step,[11] which is proposed for other iron porphyrin ORR catalysts,[60,62] measurements of i_{pl}/i_p values yield TOF_{max} values of $(2.06 \pm 0.03) \times 10^4$ s^{-1} for $[Fe_2FP]Cl_2$ and $(7 \pm 3) \times 10^1$ s^{-1} for [FeTTP]Cl. The more than 2 orders of magnitude difference between the TOF_{max} values measured using $[Fe_2FP]Cl_2$ versus [FeTTP]Cl shows the enhanced electrocatalytic activity of the fused porphyrin cannot be accounted for by a simple doubling of iron active sites per catalytic unit (*i.e.*, halving the value of TOF_{max} measured using $[Fe_2FP]Cl_2$ still yields a TOF_{max} value that is more than 2 orders of magnitude greater than that measured using [FeTTP]Cl) (see Figures S26−S28). These TOF_{max} values result in corresponding $E_{cat/2}$ values of -1.229 ± 0.006 V vs $E_{eq\,O_2/H_2O}$ and -1.174 ± 0.002 V vs $E_{eq\,O_2/H_2O}$ for $[Fe_2FP]Cl_2$ and [FeTTP]Cl, respectively. In comparison with the catalytic Tafel plot of [FeTTP]Cl—constructed from the related TOF_{max} and $E_{cat/2}$ values using the relationship given in eq 9—the catalytic Tafel plot obtained using $[Fe_2FP]Cl_2$ has no overlapping points and is shifted to the upper left of the Cartesian coordinate (Figure 6a). Further, a correlation plot of the $logTOF_{max}$ vs corresponding overpotential at $E_{cat/2}$ values shows that the benchmarks for $[Fe_2FP]Cl_2$ break the scaling relationship and deviate from the correlation slope previously measured at 54 mV/dec for a series of iron porphyrin ORR catalysts (Figure 6b).[16,63−66]

$$TOF = \frac{TOF_{max}}{1 + \exp\left[\frac{F}{RT}(E_{eq\,O_2/H_2O} - E_{cat/2})\right]\exp\left(-\frac{F}{RT}\eta\right)} \tag{9}$$

https://doi.org/10.1021/jacs.3c08586
J. Am. Chem. Soc. 2024, 146, 11622−11633

Determination of Product Distribution via Rotating Ring-Disk Electrode Analysis. ORR product distribution was investigated via rotating ring-disk electrode methods (Figure 7; see the Experimental Section for further details). In

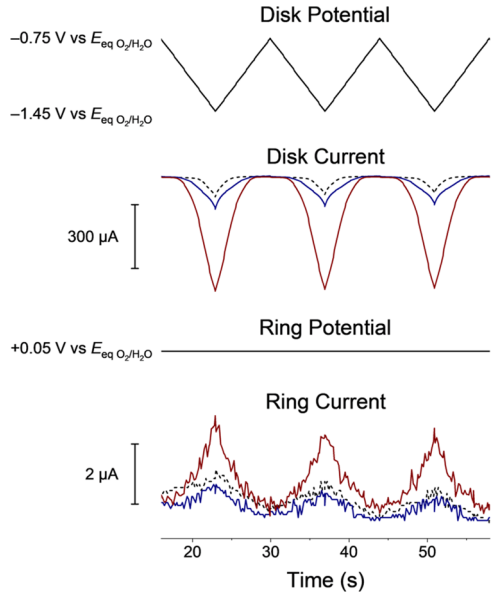

Figure 7. Rotating ring-disk electrode data recorded under O_2 (1 atm) at a scan rate of 100 mV s^{-1} and using either $[Fe_2FP]Cl_2$ (0.1 mM) (red) or [FeTTP]Cl (0.1 mM) (blue) as a catalyst, *N,N′*-dimethylformamide solutions containing $[DMFH^+][OTf^-]$ (20 mM) as a proton source, $TBAPF_6$ (0.1 M) as a supporting electrolyte, and a 5 mm diameter glassy carbon working disk electrode rotating at 1000 rpm. Currents recorded in the absence of a catalyst (black dash) are included for comparison.

these experiments, the percentage of peroxide branching (% H_2O_2) is defined as the moles of H_2O_2 produced per total moles of products (H_2O_2 and H_2O; eqs 13 and 14). Alternately, information on the fraction of current driving a specific electrochemical transformation is given by the faradaic efficiency (*FE*; eqs 16, 17, and 18). $\%H_2O_2$ and related *FE* values are plotted versus varying applied electrode potentials (ranging from −1.2 to −1.45 V vs $E_{eq\ O_2/H_2O}$) in Figures S31c and S31d, respectively. These results indicate that the averaged $\%H_2O_2$ values are 6.3% (*FE* = 3.3%) for $[Fe_2FP]Cl_2$ and 4.5% (*FE* = 2.3%) for [FeTTP]Cl. For comparison, previous reports involving structurally related iron porphyrin complexes yielded $\%H_2O_2$ values below 15%.[16]

CONCLUSIONS

We demonstrate that π-extended macrocycles provide a promising structural motif and design element for preparing electrocatalysts. We report evidence of breaking a molecular scaling relationship involving oxygen reduction catalysis. Voltammetry measurements performed using varying proton source concentrations and scan rates indicate that the iron-iron-fused porphyrin complex achieves TOF_{max} and $E_{cat/2}$ values that deviate from traditional scaling relationships and thus appear to the upper left of the conventional correlation slope obtained from catalytic Tafel plots.

The enhanced activities of binuclear molecular complexes could arise from multiple structural properties, including the electronic couplings between catalytically active sites, extended conjugation in the ligand scaffolds, through-space electrostatic stabilization of reduced intermediates by the second metal site, and cooperative binding during activation of substrates.[46] We look forward to further leveraging experimental and computational approaches in ongoing work to understand better the structure−activity relationships governing the performance of fused porphyrin catalysts, including to what extent ligand- versus metal-centered redox chemistry and spin-state effects influence the electrocatalytic reaction coordinates.

EXPERIMENTAL SECTION

Materials and Synthesis. All compounds were synthesized from commercially available starting materials. Unless noted otherwise, all reagents were purchased from commercial suppliers and used as received without further purification. Solvents were obtained from Fisher (dichloromethane, hexanes, and methanol) or Aldrich (DMF) and were distilled under nitrogen over appropriate drying reagents before use.[67] $[DMFH^+][OTf^-]$ was prepared as a white, crystalline solid following a previously reported method[68] and stored in a nitrogen dry glovebox.

[FeTTP]Cl and *meso-β* doubly fused 5,24-di(*p*-tolyl)-10,19,29,38-tetramesitylporphyrin (free-base fused porphyrin, FP) were synthesized following reported methods.[69,70] 5,10,15,20-Tetrakis[4-(trifluoromethyl)phenyl]porphyrin (T*p*CF_3PP) was synthesized via condensation of pyrrole with 4-(trifluoromethyl)benzaldehyde in the presence of BF_3 diethyl etherate using the Lindsey method.[71,72] 5,10,15,20-Tetrakis(4-methoxyphenyl)porphyrin (T*p*OMePP) was synthesized via condensation of pyrrole with 4-(methoxy)-benzaldehyde in refluxing propionic acid using the Adler−Longo method,[73] followed by treating with dichlorodicyanoquinone (DDQ) to oxidize the remaining chlorin.[74] $[Fe_2FP]Cl_2$, [FeT*p*CF_3PP]Cl, and [FeT*p*OMePP]Cl were synthesized following a modified version of a reported method[45,75,76] (see the SI for further details). The synthesized compounds were structurally characterized using matrix-assisted laser desorption/ionization time-of-flight mass spectrometry (MALDI-TOF MS), ultraviolet−visible (UV−vis) spectroscopy, Fourier transform infrared (FTIR) spectroscopy, proton nuclear magnetic resonance (^{1}H NMR) spectroscopy, and homogeneous electrochemical analysis.

Mass Spectrometry. Mass spectra were obtained using a Voyager DE STR MALDI-TOF mass spectrometer or a Bruker microFlex LRF in positive ion mode and employing *trans,trans*-1,4-diphenyl-1,3-butadiene as a matrix.

UV−vis−NIR. All ultraviolet−visible−near-infrared (UV−vis−NIR) spectra were recorded using a Shimadzu SolidSpec-3700 spectrometer with a deuterium (D_2) lamp for the ultraviolet range and a WI (halogen) lamp for the visible and near-infrared.

FITR. FTIR spectra were recorded using a Bruker Vertex 70. Unless otherwise stated, all samples were embedded in a matrix of KBr, and the spectra were collected in transmission mode using 64 scans, 1 cm^{-1} resolution, a GloBar MIR source, a broadband KBr beam splitter, and a liquid-nitrogen-cooled MCT detector. Background measurements were obtained from air, and baselines were corrected using the rubber band method. All data were processed using OPUS software.

Nuclear Magnetic Resonance. ^{1}H NMR spectra were recorded by using a Varian MR400 spectrometer operating at 400 MHz. Unless otherwise stated, all spectra were recorded at room temperature using deuterochloroform as a solvent and tetramethylsilane as an internal standard.

MicroED. Samples for MicroED analysis were prepared by adding a lacey carbon-coated EM grid to a vial containing a sample of powdered $[Fe_2FP]Cl_2$. The grid was removed; the excess powder was gently removed by tapping the tweezers holding the grid, and the grid was loaded into a Titan Krios cryo-TEM equipped with a CETA-D camera (Thermo Fisher) for MicroED data collection. Data were collected and processed using the standard MicroED methods described below. Crystals were identified on the grid using imaging

https://doi.org/10.1021/jacs.3c08586
J. Am. Chem. Soc. 2024, 146, 11622−11633

at low doses with low magnification. Initial diffraction patterns were collected in diffraction mode, and those crystals that showed quality diffraction were then used to collect full diffraction data sets using continuous rotation of the microscope stage.[77] Diffraction data were indexed, integrated, and merged using XDS,[78] with four crystals being merged into the final combined data set. The SHELX suite[79] and the ShelXle GUI[80] were used to solve and refine the structure of $[Fe_2FP]Cl_2$. Data collection and refinement statistics can be found in Table S1, and the structure has been deposited with the CCDC as entry 2264458.

Computational Methods. DFT calculations were performed with the Gaussian 16 simulation package[81] using the B3LYP functional,[82,83] including dispersion interactions with the D3 dispersion corrections based on the Becke−Johnson damping function.[84,85] The basis set included the def2tzvp basis for Fe atoms and def2svp for all other elements.[86] Geometry optimizations based on the 'Geometries, Frequencies, Noncovalent interactions extended Tight Binding' (GFN-xTB) method were performed to get approximate minimum energy structures using the standalone program provided by Grimme's group.[87] Implicit DMF solvent was included using the analytical linearized Poisson−Boltzmann model.[88] A combination of GFN-xTB and DFT was used to perform an exhaustive screening of spin states that determine Gibbs free energy differences in transition metal complexes (Tables S4 and S6).[89] A simplified model, where the *p*-methyl substituents on the phenyl rings are replaced with hydrogen atoms, was used to avoid convergence issues arising from the low energy rotation barriers of the methyl groups (see Figure S12). Table S4 reports electronic energies, free energy correction terms, and Gibbs free energies of the two different configurations in different spin states. To compare to the crystal structure, an optimization of the full model in the septet spin state and the *anti* configuration was performed as well, starting from both the crystal structure and GFN-xTB geometry. Visualizations were done using the ChimeraX program.[90−92]

Linear Sweep Voltammetry and Cyclic Voltammetry. All voltammetry measurements were performed using a Biologic SP-300 potentiostat, a glassy carbon (3 mm diameter) working electrode, a platinum counter electrode, a silver wire pseudoreference electrode, and a conventional three-electrode cell. The electrode potential of the silver wire pseudoreference electrode was determined by using the ferrocenium/ferrocene (Fc^+/Fc) redox couple as an internal standard. Electrochemical analysis grade $TBAPF_6$ electrolyte was obtained from Aldrich and stored in a desiccator containing calcium sulfate ($CaSO_4$) as a desiccant. The supporting electrolyte concentration of all electrochemical measurements was 0.1 M $TBAPF_6$, and the working electrode was cleaned between experiments by polishing with alumina (50 nm diameter) slurry, followed by rinsing with 18.2 MΩ·cm water and then acetone. The resistance of the solution between the working electrode and the reference electrode (also called the uncompensated resistance, R_u) was determined using the zero internal resistance (ZIR) technique before linear sweep voltammetry, and 85% of the uncompensated resistance was accounted for during the experiments. For kinetic analysis, the solution containing a catalyst was analyzed in the presence of $[DMFH^+][OTf^-]$ (10−100 mM) added as a freshly prepared 2 M stock solution in DMF.

Calculations of k_{cat}, TOF_{max}, $E_{cat/2}$, E_{eq}, and η. TOF_{max} values were experimentally determined using S-shaped voltammograms recorded in the presence of oxygen and an acid, where the ORR activities are limited only by the kinetics of the catalytic reaction as opposed to the diffusion of chemical substrates. The concentrations of chemical substrates and catalysts are related to the catalytic plateau current (i_{pl}) of an S-shaped voltammogram by eq 10[7,8,12−14]

$$i_{pl} = n_{cat}FAC_{cat}\sqrt{Dk_{cat}} \tag{10}$$

where n_{cat} is the number of electrons involved in the catalytic process (in this case four), A is the electrode surface area, C_{cat} is the concentration of the catalyst, and D is the diffusion coefficient for the catalyst. k_{cat} (with units of s^{-1}) is the observed, global rate constant expressed as a product of the concentrations of the chemical substrates (C_A^0) and the rate constant for catalysis (k'_{cat}, with units of $mol^{-x}\ L^x\ s^{-1}$), which takes into account the order of the reaction (x), with respect to C_A^0, as expressed in eq 3. As indicated in eq 11, catalytic currents were determined by subtracting the currents measured in the absence of a catalyst from the currents measured in the presence of a catalyst under otherwise identical experimental conditions.

$$\text{catalytic } i = i \text{ measuered with catalyst} - i \text{ measuered without catalyst} \tag{11}$$

Although this subtraction is useful to account for contributions from the increasing charging currents that accompany increasing scan rates,[93] the prevalence of the cathodic feature at applied electrode potentials more negative than ∼ −1.6 V vs $E_{eq\ O_2/H_2O}$ (recorded when using a glassy carbon working electrode either in the presence of an added catalyst or with no added catalysts) contributes to the deviation from an ideal S-shaped voltammogram waveform. Therefore, a current within the plateau-shaped region of a voltammogram response, where the first derivative of the catalytic current yields a local minimum, was selected to (1) report the corresponding catalytic plateau current, i_{pl}, and (2) identify the potential for reporting the values of catalytic currents in plots of catalytic current versus scan rate (see Section 5.4 of the Supporting Information file, regarding determinations of maximum turnover frequencies, catalytic half-wave potentials, and catalytic plateau currents, for further details).

Eq 10 can be divided by the Randles−Sevcik equation (eq 12), which describes the dependence of peak current (i_p) on the scan rate (v) for a reversible redox process measured in the absence of a chemical substrate. In the Randles−Sevcik equation, n_p represents the number of electrons involved in the redox event (in this case one).

$$i_p = 0.4463n_pFAC_{cat}\sqrt{\frac{n_pFvD}{RT}} \tag{12}$$

The i_p values were experimentally determined from the cathodic peak currents recorded in the absence of a chemical substrate at a scan rate of 100 mV s^{-1}, analyzed using a peak analysis function of the software EC-lab and a linear regression baseline. In this work, we describe the redox states of $[Fe_2FP]Cl_2$, [FeTTP]Cl, $[FeTpCF_3PP]$-Cl, and [FeTpOMePP]Cl using the monikers $[Fe_2FP]^n$, $[FeTTP]^n$, $[FeTpCF_3PP]^n$, and $[FeTpOMePP]^n$, respectively, where n gives information on the relative number of electrons transferred to or from the charge neutral $[Fe_2FP]^0$, $[FeTTP]^0$, $[FeTpCF_3PP]^0$, or $[FeTpOMePP]^0$ metalloporphyrin complex. The overlapping and electrochemically irreversible features of the $[Fe_2FP]^{2+}/[Fe_2FP]^{1+}$ and $[Fe_2FP]^{1+}/[Fe_2FP]^0$ redox couples complicate the determination of i_p. Thus, the peak current of either the $[Fe_2FP]^0/[Fe_2FP]^{1-}$, $[FeTTP]^0/[FeTTP]^{1-}$, $[FeTpCF_3PP]^0/[FeTpCF_3PP]^{1-}$, or $[FeTpOMePP]^0/[FeTpOMePP]^{1-}$ redox couple, which shows a well-separated, electrochemically reversible redox feature, was used to evaluate i_p. The resulting ratio of i_{pl}/i_p allows the determination of k_{cat} (which is equal to TOF_{max}) without independent measurement of the diffusion coefficient via eqs 7 and 8.[7,8,12−14] $E_{cat/2}$ was taken as the half-wave potential derived from plots of catalytic current versus applied electrode potential.

For the work described in this article, TOF is not affected by the concentrations of the reaction products of ORR, and changing the concentration of water in an organic solvent (including DMF) would have only a relatively small effect on the corresponding overpotentials (for example, a difference of 10 mM versus 30 mM in H_2O equates to ∼14 mV difference in overpotential). In this article, $E_{eq\ O_2/H_2O}$ is calculated using a 20 mM concentration of H_2O in DMF (consistent with a previous study reporting an average value of 20 ± 10 mM residual water in DMF as determined via Karl Fischer titration methods).[16]

The values of TOF_{max} and $E_{cat/2}$ for each catalyst were obtained via a minimum of triplicate voltammetry measurements (see Figures S21, S22, S23, and S24) and application of the relationships given in eqs 7 and 8. Using these TOF_{max} and $E_{cat/2}$ values, catalytic Tafel plots were

https://doi.org/10.1021/jacs.3c08586
J. Am. Chem. Soc. 2024, 146, 11622−11633

constructed utilizing the relationship given in eq 9. The solid lines in the catalytic Tafel plots indicate averaged values, and the shaded areas indicate standard deviations.

Deviation from the ideal S-shaped voltammogram waveform is caused by several possible side phenomena, including consumption of the chemical substrate, deactivation of the catalyst, product adsorption to the electrode surface, and background product formation at the electrode.[12] Such side phenomena complicate determinations of TOF_{max} and $E_{cat/2}$ values, and caution is advised when interpreting nonideal waveforms. Nonetheless, for the work reported herein, the variation in the values of TOF_{max} and $E_{cat/2}$ for a given catalyst (*i.e.*, $[Fe_2FP]Cl_2$, [FeTTP]Cl, $[FeTpCF_3PP]Cl$, or [FeTpOMePP]Cl) is within the experimental error of measurements over a 100 mV span of the plateau current region and has no major effect on the reported values of log TOF_{max} or $E_{cat/2}$ (see Figure S25).

Rotating Ring-Disk Electrode (RRDE) Experiments. All measurements were performed under O_2 (1 atm) using DMF solutions containing $[DMFH^+][OTf^-]$ (20 mM) as a proton source and $TBAPF_6$ (0.1 M) as a supporting electrolyte. The disk electrode was a glassy carbon disk electrode (5 mm diameter), and the ring electrode was a platinum ring electrode (purchased from Pine Research). The platinum ring electrode was polished by hand using a 3 μm diamond polishing compound on a Nylon polishing cloth, then using 1 μm diamond polishing compound on a Nylon polishing cloth, and then using 1 μm diamond polishing compound on a MicroCloth polishing pad. Following the polishing, the platinum ring electrode was rinsed with 18.2 MΩ·cm water and then sonicated in 18.2 MΩ·cm water. The potential of the glassy carbon disk electrode was swept from −0.75 V vs $E_{eq\,O_2/H_2O}$ (−0.2 V vs Fc^+/Fc) to −1.45 V vs $E_{eq\,O_2/H_2O}$ (−0.9 V vs Fc^+/Fc) at a scan rate of 100 mV s^{-1}, and the platinum ring electrode was polarized at +0.05 V vs $E_{eq\,O_2/H_2O}$ (+0.6 V vs Fc^+/Fc) to oxidize the H_2O_2 produced at the glassy carbon disk electrode. The voltammograms shown in Figures S31 and S33 were recorded before adding ferrocene as an internal standard, whereas the data shown in Figures 7 and S32 were recorded in the presence of ferrocene.

The percentage of peroxide or water branching ($\%H_2O_2$ or $\%H_2O$, respectively), defined herein as the moles of H_2O_2 or H_2O produced per total moles of products (H_2O_2 and H_2O), respectively, was calculated using eqs 13 and 14, where i_{disk} is the disk current, i_{ring} is the ring current, and N is the RRDE assembly's collection efficiency. Although eqs 13 and 14 were initially derived for heterogeneous catalysts, they can be applied to homogeneous catalysts, provided the limiting ring and disk currents are independent of rotation rate.[62] The values of i_{ring} used in eqs 13 and 14 were determined by measuring the total current at the ring electrode and subtracting the background current (*i.e.*, the ring electrode current measured when the disk electrode is polarized at potentials where no catalytic activity is observed). N was independently determined using DMF solutions containing ferrocene (1.0 mM) and by sweeping the potential of the glassy carbon working disk electrode from −0.3 to +0.5 V vs Fc^+/Fc at a scan rate of 100 mV s^{-1} to oxidize ferrocene and polarizing the platinum ring electrode at a constant potential of −0.3 V vs Fc^+/Fc to reduce the ferrocenium produced at the disk electrode (see Figure S34). These measurements to determine N were performed under an argon atmosphere in solutions containing $TBAPF_6$ (0.1 M) as the supporting electrolyte. Eq 15 was used to calculate the value of N, which is expressed as an average and using values taken from measurements recorded at rotation rates of 400, 900, 1600, and 2500 rpm and with applied electrode potentials between +0.2 and +0.5 V vs Fc^+/Fc to yield N = 22.5%.

$$\%H_2O_2 = \frac{100\left(\frac{2i_{ring}}{N}\right)}{i_{disk} + \frac{i_{ring}}{N}} \tag{13}$$

$$\%H_2O = \frac{100\left(i_{disk} - \frac{i_{ring}}{N}\right)}{i_{disk} + \frac{i_{ring}}{N}} = 100 - \%H_2O_2 \tag{14}$$

$$N = \frac{i_{ring}}{i_{disk}} \tag{15}$$

Information about the fraction of current driving a specific electrochemical transformation is given by the faradaic efficiency, *FE*, which is the ratio of the amount of chemical product (N') to the total amount of charge passed during the reaction (Q) multiplied by F and the number of electrons required to form the product (n') (eq 16). The *FE* for the formation of peroxide ($FE_{H_2O_2}$) and the *FE* for the formation of water (FE_{H_2O}) can also be calculated from $\%H_2O_2$ and $\%H_2O$ using eqs 17 and 18, respectively.

$$FE = \frac{n' \times N'(\text{mol}) \times F(C\ \text{mol}^{-1})}{Q(C)} \tag{16}$$

$$FE_{H_2O_2} = 100 \times \frac{2 \times \%H_2O_2}{2 \times \%H_2O_2 + 4 \times \%H_2O} \tag{17}$$

$$FE_{H_2O} = 100 \times \frac{4 \times \%H_2O}{2 \times \%H_2O_2 + 4 \times \%H_2O} = 100 - FE_{H_2O_2} \tag{18}$$

■ ASSOCIATED CONTENT

Supporting Information

The Supporting Information is available free of charge at https://pubs.acs.org/doi/10.1021/jacs.3c08586.

Molecular structures; molecular synthesis and characterization; MicroED data; computational analysis; electrochemical methods and additional voltammetry data; and rotating ring-disk electrode experiments data (PDF)

Accession Codes

CCDC 2264458 contains the supplementary crystallographic data for this paper. These data can be obtained free of charge via www.ccdc.cam.ac.uk/data_request/cif, or by emailing data_request@ccdc.cam.ac.uk, or by contacting The Cambridge Crystallographic Data Centre, 12 Union Road, Cambridge CB2 1EZ, UK; fax: +44 1223 336033.

■ AUTHOR INFORMATION

Corresponding Author

Gary F. Moore − *School of Molecular Sciences, Arizona State University, Tempe, Arizona 85287-1604, United States; Center for Applied Structural Discovery (CASD), The Biodesign Institute, Arizona State University, Tempe, Arizona 85281, United States;* orcid.org/0000-0003-3369-9308; Email: gfmoore@asu.edu

Authors

Daiki Nishiori − *School of Molecular Sciences, Arizona State University, Tempe, Arizona 85287-1604, United States; Center for Applied Structural Discovery (CASD), The Biodesign Institute, Arizona State University, Tempe, Arizona 85281, United States;* orcid.org/0000-0002-4707-0896

Jan Paul Menzel − *Department of Chemistry, Yale University, New Haven, Connecticut 06520-8107, United States;* orcid.org/0000-0002-1312-5000

Nicholas Armada − *School of Molecular Sciences, Arizona State University, Tempe, Arizona 85287-1604, United States; Center for Applied Structural Discovery (CASD), The*

Biodesign Institute, Arizona State University, Tempe, Arizona 85281, United States

Edgar A. Reyes Cruz − *School of Molecular Sciences, Arizona State University, Tempe, Arizona 85287-1604, United States; Center for Applied Structural Discovery (CASD), The Biodesign Institute, Arizona State University, Tempe, Arizona 85281, United States;* orcid.org/0000-0001-7307-7613

Brent L. Nannenga − *Center for Applied Structural Discovery (CASD), The Biodesign Institute, Arizona State University, Tempe, Arizona 85281, United States; Chemical Engineering, School for Engineering of Matter, Transport and Energy, Arizona State University, Tempe, Arizona 85287, United States;* orcid.org/0000-0001-6859-3429

Victor S. Batista − *Department of Chemistry, Yale University, New Haven, Connecticut 06520-8107, United States; Energy Sciences Institute, Yale University, West Haven, Connecticut 06516, United States;* orcid.org/0000-0002-3262-1237

Complete contact information is available at: https://pubs.acs.org/10.1021/jacs.3c08586

Author Contributions

This manuscript was written with contributions from all authors. All authors have approved the final version of the manuscript.

Notes

The authors declare no competing financial interest.

■ ACKNOWLEDGMENTS

This work at Arizona State University (G.F.M.) was supported by the US Department of Energy, Office of Science, Office of Basic Energy Sciences, under Early Career Award DE-SC0021186. G.F.M. also acknowledges support from the Camille Dreyfus Teacher-Scholar Awards Program. G.F.M. also acknowledges the NIH grant 1S10OD032472-01 for the use of Rapiflex MALDI-TOF/TOF instrument. B.L.N. acknowledges the funding support by the National Science Foundation (DMR-1942084). This work at Yale University (V.S.B.) was supported by the US Department of Energy, Chemical Sciences, Geosciences, and Biosciences Division, Office of Basic Energy Sciences, Office of Science (Grant DE-FG02-07ER15909). D.N. acknowledges support from the Completion Fellowship from the Graduate College, Arizona State University. NMR studies were performed using the Magnetic Resonance Research Center at Arizona State University. MALDI-TOF data were collected at the Mass Spectrometry Facility in the Biodesign Institute at Arizona State University.

■ REFERENCES

(1) Pérez-Ramírez, J.; López, N. Strategies to Break Linear Scaling Relationships. *Nat. Catal.* **2019**, *2*, 971−976.

(2) Masa, J.; Schuhmann, W. Breaking Scaling Relations in Electrocatalysis. *J. Solid State Electrochem.* **2020**, *24*, 2181−2182.

(3) Nie, W.; McCrory, C. C. L. Strategies for Breaking Molecular Scaling Relationships for the Electrochemical CO_2 Reduction Reaction. *Dalton Trans.* **2022**, *51*, 6993−7010.

(4) Kulkarni, A.; Siahrostami, S.; Patel, A.; Nørskov, J. K. Understanding Catalytic Activity Trends in the Oxygen Reduction Reaction. *Chem. Rev.* **2018**, *118*, 2302−2312.

(5) Sabatier, P. Hydrogénations et Déshydrogénations Par Catalyse. *Ber. Dtsch. Chem. Ges.* **1911**, *44*, 1984−2001.

(6) Bligaard, T.; Nørskov, J. K.; Dahl, S.; Matthiesen, J.; Christensen, C. H.; Sehested, J. The Brønsted−Evans−Polanyi Relation and the Volcano Curve in Heterogeneous Catalysis. *J. Catal.* **2004**, *224*, 206−217.

(7) Artero, V.; Savéant, J.-M. Toward the Rational Benchmarking of Homogeneous H_2-Evolving Catalysts. *Energy Environ. Sci.* **2014**, *7*, 3808−3814.

(8) Costentin, C.; Savéant, J.-M. Multielectron, Multistep Molecular Catalysis of Electrochemical Reactions: Benchmarking of Homogeneous Catalysts. *ChemElectroChem* **2014**, *1*, 1226−1236.

(9) Roberts, J. A. S.; Bullock, R. M. Direct Determination of Equilibrium Potentials for Hydrogen Oxidation/Production by Open Circuit Potential Measurements in Acetonitrile. *Inorg. Chem.* **2013**, *52*, 3823−3835.

(10) Stratakes, B. M.; Dempsey, J. L.; Miller, A. J. M. Determining the Overpotential of Electrochemical Fuel Synthesis Mediated by Molecular Catalysts: Recommended Practices, Standard Reduction Potentials, and Challenges. *ChemElectroChem* **2021**, *8*, 4161−4180.

(11) Pegis, M. L.; Wise, C. F.; Martin, D. J.; Mayer, J. M. Oxygen Reduction by Homogeneous Molecular Catalysts and Electrocatalysts. *Chem. Rev.* **2018**, *118*, 2340−2391.

(12) Rountree, E. S.; McCarthy, B. D.; Eisenhart, T. T.; Dempsey, J. L. Evaluation of Homogeneous Electrocatalysts by Cyclic Voltammetry. *Inorg. Chem.* **2014**, *53*, 9983−10002.

(13) Costentin, C.; Drouet, S.; Robert, M.; Savéant, J.-M. Turnover Numbers, Turnover Frequencies, and Overpotential in Molecular Catalysis of Electrochemical Reactions. Cyclic Voltammetry and Preparative-Scale Electrolysis. *J. Am. Chem. Soc.* **2012**, *134*, 11235−11242.

(14) Lee, K. J.; Elgrishi, N.; Kandemir, B.; Dempsey, J. L. Electrochemical and Spectroscopic Methods for Evaluating Molecular Electrocatalysts. *Nat. Rev. Chem.* **2017**, *1*, No. 0039.

(15) Appel, A. M.; Helm, M. L. Determining the Overpotential for a Molecular Electrocatalyst. *ACS Catal.* **2014**, *4*, 630−633.

(16) Pegis, M. L.; McKeown, B. A.; Kumar, N.; Lang, K.; Wasylenko, D. J.; Zhang, X. P.; Raugei, S.; Mayer, J. M. Homogenous Electrocatalytic Oxygen Reduction Rates Correlate with Reaction Overpotential in Acidic Organic Solutions. *ACS Cent. Sci.* **2016**, *2*, 850−856.

(17) Azcarate, I.; Costentin, C.; Robert, M.; Savéant, J.-M. Dissection of Electronic Substituent Effects in Multielectron-Multistep Molecular Catalysis. Electrochemical CO_2-to-CO Conversion Catalyzed by Iron Porphyrins. *J. Phys. Chem. C* **2016**, *120*, 28951−28960.

(18) Costentin, C.; Savéant, J.-M. Homogeneous Molecular Catalysis of Electrochemical Reactions: Catalyst Benchmarking and Optimization Strategies. *J. Am. Chem. Soc.* **2017**, *139*, 8245−8250.

(19) Costentin, C.; Savéant, J.-M. Homogeneous Molecular Catalysis of Electrochemical Reactions: Manipulating Intrinsic and Operational Factors for Catalyst Improvement. *J. Am. Chem. Soc.* **2018**, *140*, 16669−16675.

(20) Costentin, C.; Savéant, J.-M. Towards an Intelligent Design of Molecular Electrocatalysts. *Nat. Rev. Chem.* **2017**, *1*, No. 87.

(21) Reyes Cruz, E. A.; Nishiori, D.; Wadsworth, B. L.; Nguyen, N. P.; Hensleigh, L. K.; Khusnutdinova, D.; Beiler, A. M.; Moore, G. F. Molecular-Modified Photocathodes for Applications in Artificial Photosynthesis and Solar-to-Fuel Technologies. *Chem. Rev.* **2022**, *122*, 16051−16109.

(22) Nishiori, D.; Wadsworth, B. L.; Moore, G. F. Parallels between Enzyme Catalysis, Electrocatalysis, and Photoelectrosynthesis. *Chem. Catal.* **2021**, *1*, 978−996.

(23) Nocera, D. G. Solar Fuels and Solar Chemicals Industry. *Acc. Chem. Res.* **2017**, *50*, 616−619.

(24) Marcus, R. A. On the Theory of Electron-Transfer Reactions. VI. Unified Treatment for Homogeneous and Electrode Reactions. *J. Chem. Phys.* **1965**, *43*, 679−701.

(25) Piechota, E. J.; Meyer, G. J. Introduction to Electron Transfer: Theoretical Foundations and Pedagogical Examples. *J. Chem. Educ.* **2019**, *96*, 2450−2466.

(26) Mayer, J. M. Proton-Coupled Electron Transfer: A Reaction Chemist's View. *Annu. Rev. Phys. Chem.* **2004**, *55*, 363−390.

(27) Huynh, M. H. V.; Meyer, T. J. Proton-Coupled Electron Transfer. *Chem. Rev.* **2007**, *107*, 5004−5064.
(28) Savéant, J.-M. Concerted Proton-Electron Transfers: Fundamentals and Recent Developments. *Annu. Rev. Anal. Chem.* **2014**, *7*, 537−560.
(29) Tumas, B.; Dempsey, J.; Mollouk, T.; Ardo, S.; Bren, K.; Rappe, A.; Shaw, W.; Abruna, H.; Atwater, H.; Ayers, K.; Berlinguette, C.; Concepcion, J.; Cooper, V.; Esposito, D.; Gregorie, J.; Hammarstrom, L.; Haussener, S.; Houle, F.; Linic, S.; Shafaat, H.; Shao-Horn, Y.; Smith, W.; Surendranath, Y.; Tiede, D.; Yang, J. *Report of the Basic Energy Sciences Roundtable on Liquid Solar Fuels*; U.S. Department of Energy, 2019.
(30) Ager, J.; Deutsch, T.; Esposito, D.; Gregoire, J.; Hahn, C.; Hammarström, L.; Jaramillo, T.; King, L.; King, P.; Miller, D.; Miller-Link, E.; Moore, G.; Mulfort, K.; Neale, N.; Nozik, A.; Osterloh, F.; Ozin, G.; Peters, J.; Polyanski, D.; Seefeldt, L.; Smith, W.; Xiang, C.; Yu, J. *Facual Document for the BES Roundtable on Liquid Solar Fuels*; U.S. Department of Energy, 2019.
(31) Helm, M. L.; Stewart, M. P.; Bullock, R. M.; Dubois, M. R.; Dubois, D. L. A Synthetic Nickel Electrocatalyst with a Turnover Frequency Above 100,000 s^{-1} for H_2 Production. *Science* **2011**, *333*, 863−866.
(32) Costentin, C.; Passard, G.; Robert, M.; Savéant, J.-M. Pendant Acid-Base Groups in Molecular Catalysts: H-Bond Promoters or Proton Relays? Mechanisms of the Conversion of CO_2 to CO by Electrogenerated Iron(0) Porphyrins Bearing Prepositioned Phenol Functionalities. *J. Am. Chem. Soc.* **2014**, *136*, 11821−11829.
(33) Bhunia, S.; Ghatak, A.; Dey, A. Second Sphere Effects on Oxygen Reduction and Peroxide Activation by Mononuclear Iron Porphyrins and Related Systems. *Chem. Rev.* **2022**, *122*, 12370−12426.
(34) McGuire Jr, R.; Dogutan, D. K.; Teets, T. S.; Suntivich, J.; Shao-Horn, Y.; Nocera, D. G. Oxygen Reduction Reactivity of Cobalt(II) Hangman Porphyrins. *Chem. Sci.* **2010**, *1*, 411−414.
(35) Passard, G.; Dogutan, D. K.; Qiu, M.; Costentin, C.; Nocera, D. G. Oxygen Reduction Reaction Promoted by Manganese Porphyrins. *ACS Catal.* **2018**, *8*, 8671−8679.
(36) Azcarate, I.; Costentin, C.; Robert, M.; Savéant, J.-M. Through-Space Charge Interaction Substituent Effects in Molecular Catalysis Leading to the Design of the Most Efficient Catalyst of CO_2-to-CO Electrochemical Conversion. *J. Am. Chem. Soc.* **2016**, *138*, 16639−16644.
(37) Martin, D. J.; Johnson, S. I.; Mercado, B. Q.; Raugei, S.; Mayer, J. M. Intramolecular Electrostatic Effects on O_2, CO_2, and Acetate Binding to a Cationic Iron Porphyrin. *Inorg. Chem.* **2020**, *59*, 17402−17414.
(38) Martin, D. J.; Mayer, J. M. Oriented Electrostatic Effects on O_2 and CO_2 Reduction by a Polycationic Iron Porphyrin. *J. Am. Chem. Soc.* **2021**, *143*, 11423−11434.
(39) Gonell, S.; Massey, M. D.; Moseley, I. P.; Schauer, C. K.; Muckerman, J. T.; Miller, A. J. M. Trans Effect in Electrocatalytic CO2 Reduction: Mechanistic Studies of Asymmetric Ruthenium Pyridyl-Carbene Catalysts. *J. Am. Chem. Soc.* **2019**, *141*, 6658−6671.
(40) Gonell, S.; Assaf, E. A.; Du, K. D.; Schauer, C. K.; Miller, A. J. M. Kinetics of the Trans Effect in Ruthenium Complexes Provide Insight into the Factors That Control Activity and Stability in CO2 Electroreduction. *J. Am. Chem. Soc.* **2020**, *142*, 8980−8999.
(41) Wilkinson, A. D.; McNaught, A. *IUPAC Compendium of Chemical Terminology*, 3rd ed.; International Union of Pure and Applied Chemistry: Online version 3.0.1, 2019.
(42) Khusnutdinova, D.; Wadsworth, B. L.; Flores, M.; Beiler, A. M.; Reyes Cruz, E. A.; Zenkov, Y.; Moore, G. F. Electrocatalytic Properties of Binuclear Cu(II) Fused Porphyrins for Hydrogen Evolution. *ACS Catal.* **2018**, *8*, 9888−9898.
(43) Fokin, I.; Siewert, I. Chemoselective Electrochemical Hydrogenation of Ketones and Aldehydes with a Well-Defined Base-Metal Catalyst. *Chem. - Eur. J.* **2020**, *26*, 14137−14143.
(44) Nie, W.; Tarnopol, D. E.; McCrory, C. C. L. Enhancing a Molecular Electrocatalyst's Activity for CO_2 Reduction by Simultaneously Modulating Three Substituent Effects. *J. Am. Chem. Soc.* **2021**, *143*, 3764−3778.
(45) Reyes Cruz, E. A.; Nishiori, D.; Wadsworth, B. L.; Khusnutdinova, D.; Karcher, T.; Landrot, G.; Lassalle-Kaiser, B.; Moore, G. F. Six-Electron Chemistry of a Binuclear Fe(III) Fused Porphyrin. *ChemElectroChem.* **2021**, *8*, 3614−3620.
(46) Nie, W.; Tarnopol, D. E.; McCrory, C. C. L. The Effect of Extended Conjugation on Electrocatalytic CO_2 Reduction by Molecular Catalysts and Macromolecular Structures. *Curr. Opin. Electrochem.* **2021**, *28*, No. 100716.
(47) Tsuda, A.; Furuta, H.; Osuka, A. Syntheses, Structural Characterizations, and Optical and Electrochemical Properties of Directly Fused Diporphyrins. *J. Am. Chem. Soc.* **2001**, *123*, 10304−10321.
(48) Hazari, A. S.; Chandra, S.; Kar, S.; Sarkar, B. Metal Complexes of Singly, Doubly and Triply Linked Porphyrins and Corroles: An Insight into the Physicochemical Properties. *Chem. - Eur. J.* **2022**, *28*, No. e202104550.
(49) Augustyn, V.; Berman, D.; Chen, Q.; Cui, Y.; DeYoreo, J.; Gu, X.; Idrobo, J. C.; Jungjohann, K.; Kourkoutis, L.; Liu, A.; McComb, D.; Moore, G.; Nelson, H.; Ross, F.; Stemmer, S.; Streubel, R.; Wallace, A.; Wang, C.; Yan, H.; Yang, P. *Report of the Basic Energy Sciences Roundtable on Research Opportunities in the Physical Sciences Enabled by Cryogenic Electron Microscopy*; U.S. Department of Energy, 2021.
(50) Nannenga, B. L.; Gonen, T. The Cryo-EM Method Microcrystal Electron Diffraction (MicroED). *Nat. Methods* **2019**, *16*, 369−379.
(51) Scheidt, B. Y. W. R.; Finnegan, M. G. Structure of Monoclinic Chloro(Meso-Tetraphenylporphyrinato)Iron(III). *J. Appl. Crystallogr.* **1989**, *45*, 1214−1216.
(52) Scheidt, W. R.; Reed, C. A. Spin-State/Stereochemical Relationships in Iron Porphyrins: Implications for the Hemoproteins. *Chem. Rev.* **1981**, *81*, 543−555.
(53) Sahoo, D.; Quesne, M. G.; De Visser, S. P.; Rath, S. P. Hydrogen-Bonding Interactions Trigger a Spin-Flip in Iron(III) Porphyrin Complexes. *Angew. Chem., Int. Ed.* **2015**, *54*, 4796−4800.
(54) Nakamura, M. Electronic Structures of Highly Deformed Iron(III) Porphyrin Complexes. *Coord. Chem. Rev.* **2006**, *250*, 2271−2294.
(55) Savéant, J.-M.; Su, K. B. Homogeneous Redox Catalysis of Electrochemical Reaction. Part VI. Zone Diagram Representation of the Kinetic Regimes. *J. Electroanal. Chem.* **1984**, *171*, 341−349.
(56) Crabtree, R. H. Resolving Heterogeneity Problems and Impurity Artifacts in Operationally Homogeneous Transition Metal Catalysts. *Chem. Rev.* **2012**, *112*, 1536−1554.
(57) Artero, V.; Fontecave, M. Solar Fuels Generation and Molecular Systems: Is It Homogeneous or Heterogeneous Catalysis? *Chem. Soc. Rev.* **2013**, *42*, 2338−2356.
(58) Lee, K. J.; McCarthy, B. D.; Dempsey, J. L. On Decomposition, Degradation, and Voltammetric Deviation: The Electrochemist's Field Guide to Identifying Precatalyst Transformation. *Chem. Soc. Rev.* **2019**, *48*, 2927−2945.
(59) James, H. J.; Broman, R. F. Modified Winkler Determination of Oxygen in Dimethylformamide: Oxygen Solubility as a Function of Partial Pressure. *Anal. Chim. Acta* **1969**, *48*, 411−417.
(60) Wasylenko, D. J.; Rodríguez, C.; Pegis, M. L.; Mayer, J. M. Direct Comparison of Electrochemical and Spectrochemical Kinetics for Catalytic Oxygen Reduction. *J. Am. Chem. Soc.* **2014**, *136*, 12544−12547.
(61) Klug, C. M.; Dougherty, W. G.; Kassel, W. S.; Wiedner, E. S. Electrocatalytic Hydrogen Production by a Nickel Complex Containing a Tetradentate Phosphine Ligand. *Organometallics* **2019**, *38*, 1269−1279.
(62) Pegis, M. L.; Martin, D. J.; Wise, C. F.; Brezny, A. C.; Johnson, S. I.; Johnson, L. E.; Kumar, N.; Raugei, S.; Mayer, J. M. Mechanism of Catalytic O_2 Reduction by Iron Tetraphenylporphyrin. *J. Am. Chem. Soc.* **2019**, *141*, 8315−8326.

https://doi.org/10.1021/jacs.3c08586
J. Am. Chem. Soc. 2024, 146, 11622−11633

(63) Pegis, M. L.; Wise, C. F.; Koronkiewicz, B.; Mayer, J. M. Identifying and Breaking Scaling Relations in Molecular Catalysis of Electrochemical Reactions. *J. Am. Chem. Soc.* **2017**, *139*, 11000−11003.
(64) Martin, D. J.; Wise, C. F.; Pegis, M. L.; Mayer, J. M. Developing Scaling Relationships for Molecular Electrocatalysis through Studies of Fe-Porphyrin-Catalyzed O_2 Reduction. *Acc. Chem. Res.* **2020**, *53*, 1056−1065.
(65) Martin, D. J.; Mercado, B. Q.; Mayer, J. M. Combining Scaling Relationships Overcomes Rate versus Overpotential Trade-Offs in O_2 Molecular Electrocatalysis. *Sci. Adv.* **2020**, *6*, No. eaaz3318.
(66) Groff, B. D.; Mayer, J. M. Optimizing Catalysis by Combining Molecular Scaling Relationships: Iron Porphyrin-Catalyzed Electrochemical Oxygen Reduction as a Case Study. *ACS Catal.* **2022**, *12*, 11692−11696.
(67) Chai, C.; Armarego, W. L. F. *Purification of Laboratory Chemicals*, 5thth ed.; Butterworth-Heinemann, 2003; pp 1−608.
(68) Favier, I.; Duñach, E. New Protic Salts of Aprotic Polar Solvents. *Tetrahedron Lett.* **2004**, *45*, 3393−3395.
(69) Khusnutdinova, D.; Beiler, A. M.; Wadsworth, B. L.; Jacob, S. I.; Moore, G. F. Metalloporphyrin-Modified Semiconductors for Solar Fuel Production. *Chem. Sci.* **2017**, *8*, 253−259.
(70) Brennan, B. J.; Arero, J.; Liddell, P. A.; Moore, T. A.; Moore, A. L.; Gust, D. Selective Oxidative Synthesis of Meso-Beta Fused Porphyrin Dimers. *J. Porphyrins Phthalocyanines* **2013**, *17*, 247−251.
(71) Lindsey, J. S.; Hsu, H. C.; Schreiman, I. C. Synthesis of Tetraphenylporphyrins under Very Mild Conditions. *Tetrahedron Lett.* **1986**, *27*, 4969−4970.
(72) Kooriyaden, F. R.; Sujatha, S.; Arunkumar, C. Synthesis, Spectral, Structural and Antimicrobial Studies of Fluorinated Porphyrins. *Polyhedron* **2015**, *97*, 66−74.
(73) Adler, A. D.; Longo, F. R.; Finarelli, J. D.; Goldmacher, J.; Assour, J.; Korsakoff, L. A Simplified Synthesis for Meso-Tetraphenylporphine. *J. Org. Chem.* **1967**, *32*, 476.
(74) Barnett, G. H.; Hudson, M. F.; Smith, K. M. Concerning Meso-Tetraphenylporphyrin Purification. *J. Chem. Soc., Perkin Trans. 1* **1975**, *1*, 1401−1403.
(75) Tabor, E.; Połtowicz, J.; Pamin, K.; Basąg, S.; Kubiak, W. Influence of Substituents in Meso-Aryl Groups of Iron μ-Oxo Porphyrins on Their Catalytic Activity in the Oxidation of Cycloalkanes. *Polyhedron* **2016**, *119*, 342−349.
(76) Asano, N.; Uemura, S.; Kinugawa, T.; Akasaka, H.; Mizutani, T. Synthesis of Biladienone and Bilatrienone by Coupled Oxidation of Tetraarylporphyrins. *J. Org. Chem.* **2007**, *72*, 5320−5326.
(77) Nannenga, B. L.; Shi, D.; Leslie, A. G. W.; Gonen, T. High-Resolution Structure Determination by Continuous-Rotation Data Collection in MicroED. *Nat. Methods* **2014**, *11*, 927−930.
(78) Kabsch, W. XDS. *Acta Crystallogr., Sect. D: Biol. Crystallogr.* **2010**, *66*, 125−132.
(79) Sheldrick, G. M. SHELXT − Integrated Space-Group and Crystal-Structure Determination. *Acta Crystallogr., Sect. A: Found. Adv.* **2015**, *71*, 3−8.
(80) Hübschle, C. B.; Sheldrick, G. M.; Dittrich, B. ShelXle: A Qt Graphical User Interface for SHELXL. *J. Appl. Crystallogr.* **2011**, *44*, 1281−1284.
(81) Frisch, M. J.; Trucks, G. W.; Schlegel, H. B.; Scuseria, G. E.; Robb, M. A.; Cheeseman, J. R.; Scalmani, G.; Barone, V.; Petersson, G. A.; Nakatsuji, H.; Li, X.; Caricato, M.; Marenich, A. V.; Bloino, J.; Janesko, B. G.; Gomperts, R.; Mennucci, B.; Hratchian, H. P.; Ortiz, J. V. et al. *Gaussian 16*, Rev. C.01; Gaussian Inc.: Wallingford, CT, 2016.
(82) Becke, A. D. A New Mixing of Hartree−Fock and Local Density-functional Theories. *J. Chem. Phys.* **1993**, *98*, 1372−1377.
(83) Lee, C.; Yang, W.; Parr, R. G. Development of the Colle-Salvetti Correlation-Energy Formula into a Functional of the Electron Density. *Phys. Rev. B* **1988**, *37*, 785−789.
(84) Grimme, S.; Antony, J.; Ehrlich, S.; Krieg, H. A Consistent and Accurate Ab Initio Parametrization of Density Functional Dispersion Correction (DFT-D) for the 94 Elements H-Pu. *J. Chem. Phys.* **2010**, *132*, No. 154104.
(85) Grimme, S.; Ehrlich, S.; Goerigk, L. Effect of the Damping Function in Dispersion Corrected Density Functional Theory. *J. Comput. Chem.* **2011**, *32*, 1456−1465.
(86) Weigend, F.; Ahlrichs, R. Balanced Basis Sets of Split Valence, Triple Zeta Valence and Quadruple Zeta Valence Quality for H to Rn: Design and Assessment of Accuracy. *Phys. Chem. Chem. Phys.* **2005**, *7*, 3297−3305.
(87) Grimme, S.; Bannwarth, C.; Shushkov, P. A Robust and Accurate Tight-Binding Quantum Chemical Method for Structures, Vibrational Frequencies, and Noncovalent Interactions of Large Molecular Systems Parametrized for All Spd-Block Elements (Z = 1−86). *J. Chem. Theory Comput.* **2017**, *13*, 1989−2009.
(88) Ehlert, S.; Stahn, M.; Spicher, S.; Grimme, S. Robust and Efficient Implicit Solvation Model for Fast Semiempirical Methods. *J. Chem. Theory Comput.* **2021**, *17*, 4250−4261.
(89) Menzel, J. P.; Kloppenburg, M.; Belić, J.; de Groot, H. J. M.; Visscher, L.; Buda, F. Efficient Workflow for the Investigation of the Catalytic Cycle of Water Oxidation Catalysts: Combining GFN-xTB and Density Functional Theory. *J. Comput. Chem.* **2021**, *42*, 1885−1894.
(90) Humphrey, W.; Dalke, A.; Schulten, K. VMD: Visual Molecular Dynamics. *J. Mol. Graphics* **1996**, *14*, 33−38.
(91) Goddard, T. D.; Huang, C. C.; Meng, E. C.; Pettersen, E. F.; Couch, G. S.; Morris, J. H.; Ferrin, T. E. UCSF ChimeraX: Meeting Modern Challenges in Visualization and Analysis. *Protein Sci.* **2018**, *27*, 14−25.
(92) Pettersen, E. F.; Goddard, T. D.; Huang, C. C.; Meng, E. C.; Couch, G. S.; Croll, T. I.; Morris, J. H.; Ferrin, T. E. UCSF ChimeraX: Structure Visualization for Researchers, Educators, and Developers. *Protein Sci.* **2021**, *30*, 70−82.
(93) Bard, A. J.; Faulkner, L. R. *Electrochemical Methods: Fundamentals and Applications*, 2nd ed.; John Wiley & Sons, Inc: New York, 2001.

https://doi.org/10.1021/jacs.3c08586
J. Am. Chem. Soc. 2024, 146, 11622−11633